Available online at www.sciencedirect.com

ScienceDirect

Journal of the Franklin Institute 356 (2019) 5001–5026

www.elsevier.com/locate/jfranklin

New approach to visual servo control using terminal constraints☆

S.S. Mehta[a,*], C. Ton[b], M. Rysz[c], Z. Kan[d], E.A. Doucette[e], J.W. Curtis[e]

[a] *Department of Mechanical and Aerospace Engineering, University of Florida, Shalimar, FL USA*
[b] *Air Force Research Laboratory, Space Vehicles Directorate, Kirtland AFB, NM USA*
[c] *Department of Industrial and Systems Engineering, University of Florida, Shalimar, FL USA*
[d] *Department of Mechanical Engineering, University of Iowa, Iowa City, IA USA*
[e] *Air Force Research Laboratory, Munitions Directorate, Eglin AFB, FL USA*

Received 7 August 2018; received in revised form 11 March 2019; accepted 27 April 2019
Available online 9 May 2019

Abstract

A large class of visual servo controllers relies on an *a priori* obtained reference image, captured at the desired position and orientation (i.e., pose) of a camera, to yield control signals to regulate the camera from its current pose to a desired pose. In many applications, accessibility and economics of the operation may prohibit acquisition of such a reference image. This paper introduces a new visual servo control paradigm that enables control of the camera in the absence of reference image using a set of terminal constraints. Specifically, the desired pose is encoded using the *angle of obliquity* of the optical axis with respect to the object plane and its *direction of arrival* at the plane. A constrained convex optimization problem is formulated over a conic section defined by the terminal constraints to yield an error system for the control problem. Subsequently, this work introduces continuous terminal sliding mode visual servo controllers to regulate the camera to the desired pose. Lyapunov-based stability

☆ This research is supported in part by the US Air Force Research Laboratory contracts #FA8651-08-D-0108/049-050, #FA8651-16-2-0009, #FA-87651-19-F-1010 and the United States Department of Agriculture Small Business Innovation Research award USDA NIFA SBIR #2016-33610-25473. Any opinions, findings and conclusions or recommendations expressed in this material are those of the author(s) and do not necessarily reflect the views of the funding agency.

* Corresponding author.
E-mail address: siddhart@ufl.edu (S.S. Mehta).

https://doi.org/10.1016/j.jfranklin.2019.04.026

analysis guarantees that the origin is a finite-time-stable equilibrium of the system. Numerical simulation results are provided to verify the performance of the proposed visual servo controller.

1. Introduction

Visual servo controllers can be broadly classified into image-based visual servo (IBVS) controllers, position-based visual servo (PBVS) controllers, and hybrid visual servo controllers. In IBVS, control signals are derived based on the difference between the current and the desired position of the object features in the image plane and by mapping the task-space camera velocities into the image-space feature velocities using an image Jacobian [1,2]. However, since no Euclidean information of the object position and orientation (i.e., pose) is included in the controller development, IBVS may induce large and infeasible camera motion [3]. PBVS, on the contrary, estimates Euclidean pose of the object with respect to the camera using knowledge of the object's model or by knowing the camera motion and designs control signals based on the estimated task-space object pose [1,2,4]. As PBVS is defined in terms of task-space coordinates, image-space regulation of the features cannot guaranteed. Hybrid visual servo controllers, such as 2.5D visual servo control [5], partitioned IBVS [3] and approaches in [6,7], fuse IBVS and PBVS methods to eliminate their individual shortcomings by obtaining control signals using image measurements and partial Euclidean reconstruction of the object. Within the class of hybrid controllers, 2.5D visual servo controller is widely studied in part due to its stability guarantees (e.g., [8–21] and the references therein).

A typical 2.5D visual servoing problem is constructed as a *teach by showing* (TBS) problem. In TBS, a camera is *a priori* positioned at the desired location to acquire a "reference image", which encodes the desired pose of the camera with respect to the object as shown in Fig. 1 – hence the name 'teach by showing'. The camera is then manually moved back to its initial pose to capture its current view of the object. The control objective becomes to reposition the camera at the desired location by means of visual servo control [1,2,5,22]. To determine the camera motion, the relationship between the current and the reference images is obtained by computing the homography between the two images using the epipolar geometry of the camera. By decomposing the homography, the rotation and the (scaled) translation between the two viewpoints can be obtained. The obtained rotation enables design of the angular velocity of the camera while the translation component together with the computed relative depth information can be used to obtain the linear velocity of the camera. For many applications, however, it may not be feasible to acquire a reference image by *a priori* positioning a camera at the desired location. Such applications may include image-guided weapon systems, robotic hazardous material handling, robotic fruit harvesting, and unstructured manufacturing facilities, where the classical 2.5D visual servo control framework based on homography obtained using the current and the reference image may be prohibitive. A teach by zooming (TBZ) visual servo controller, that does not rely on the TBS paradigm of positioning the camera at the desired location, was presented in our prior work [21]. In TBZ, the reference image encoding the desired pose of the camera was obtained using another camera with zooming capabilities. For example, a camera mounted on a satellite zooms on to an object to acquire a reference image. Subsequently, error dynamics were formulated based

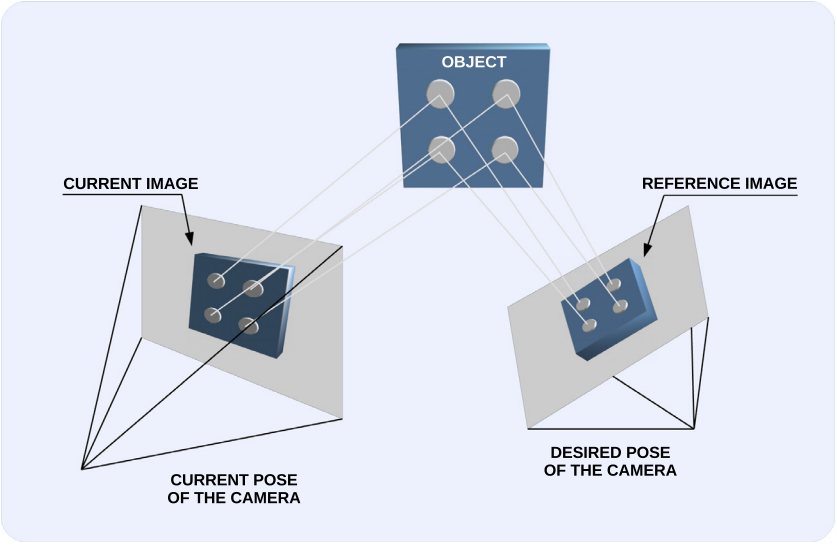

Fig. 1. Teach by showing paradigm showing the current and the reference images of an object captured by the camera.

on 2.5D visual servo control principles to obtain control signals with an objective to match the current image captured by the non-zooming camera with the reference image acquired by the zooming camera. Although the TBZ framework does not require positioning a camera at the desired location, a reference image encoding the desired pose is necessary. In applications, such as robotic fruit harvesting, acquiring a reference image for each fruit to be harvested can be impractical and may adversely affect harvesting economics and fruit picking efficiency.

Leveraging on our preliminary work in [23], a new 2.5D visual servo controller is presented that does not rely on a reference image. The problem is motivated by applications where a desired pose of the camera is defined in terms of a set of terminal constraints instead of a reference image. For example, an autonomous weapon may be required to impact a target at an orientation that maximizes target penetration [24,25], while avoiding being detected, thereby establishing constraints on terminal ballistics. In autonomous fruit harvesting [26,27], the orientation of the robot end-effector with respect to the fruit stem is critical to the success of fruit detachment [28]. In autonomous landing [29,30], an approach angle and the wind direction may dictate the desired orientation of an aircraft at landing. Manufacturing and production processes that require autonomous object manipulation and grasping [31–33] rely on precise orientation of the tool with respect to the workpiece. Inspired by such applications, terminal constraints are considered to encode the desired orientation of the camera and are defined using the desired *angle of obliquity* and the desired *direction of arrival* of the camera at the object plane. The angle of obliquity condition, defined as the angle between the camera's optical axis and the object plane, represents a pencil of lines[1] describing the surface of a right

[1] In the presented formulation, a pencil of lines refers to a set of lines drawn from the camera that intercept the planar object at the desired angle of obliquity. These lines form the lateral surface of a right circular cone with its apex at the camera and base on the object plane. Alternatively, the pencil of lines represents the generatrix (i.e., the line segments drawn from the apex of the cone to the perimeter of the base of the cone) of the lateral surface of the cone. This fact will be exploited to develop a rotation controller for the camera that satisfies the terminal constraints.

circular cone. Consequently, the generatrix lines of the cone identify possible orientations of the optical axis. Further, the desired direction of arrival may indicate an angle or, in general, a range of angles (e.g., $(0, \pi/3] \cup [2\pi/3, \pi]$) of the optical axis with respect to a reference direction (e.g., local north) in the object plane. Same as the angle of obliquity, the concept of direction of arrival is motivated by practical applications. For example, the direction of arrival can be selected to avoid obstacles (e.g., branches and trunk) in robotic fruit harvesting, to avoid being detected in autonomous weapon systems, or to land an aircraft with headwind. Further, the concepts from Euclidean geometry are utilized to establish a relationship between the current pose of the camera and the terminal constraints. Since the terminal constraints may not define a unique orientation of the camera, an optimal desired orientation that minimizes camera motion is obtained by solving a constrained convex optimization problem on a conic section formed by the terminal constraints. By virtue of novel angular mappings, an efficient algorithmic solution can be obtained to the optimization problem. Thereupon, a 2.5D visual servo control problem is posed considering decoupled rotation and translation control, and continuous terminal sliding mode controllers are introduced. In contrast to existing 2.5D controllers [14,21,23], the developed controllers guarantee that the current pose of the camera is regulated to the desired pose in *finite-time*. Extensive simulation results are provided that validate the performance of the developed controller.

The main contribution of the paper is in the development of a new terminal constraints based approach to 2.5D visual servo control that does not rely on a reference image. As such, the presented control paradigm is not only more practical but also provides greater operational flexibility since any change in the desired pose can easily be accommodated without requiring to recapture a new reference image. Through novel geometric formulations the terminal constraints are expressed in a form that is amenable to the classical 2.5D visual servo control, where the challenge associated with under-constrained desired orientation is addressed by solving a constrained convex optimization problem using the presented efficient algorithmic solution. Finally, to the best knowledge of the authors, the presented result is the first to introduce terminal sliding mode control for 2.5D visual servo control systems to enable stronger - finite-time - convergence guarantees.

The paper is organized as follows: The geometric relationships between the camera coordinate frames and the object are developed in Section 2. The concepts of angle of obliquity and direction of arrival are formally introduced in Section 3 to facilitate development of terminal constraints. With an objective to achieve a desired pose defined by the terminal constraints, rotation and translation controllers are developed and analyzed in Section 4. Section 5 demonstrates the performance of the controllers through numerical simulations.

2. Euclidean reconstruction

Consider orthogonal coordinate frames $\mathcal{F}$, $\mathcal{F}^*$, and $\mathcal{F}_t$ as shown in Fig. 2. The time-varying coordinate frame $\mathcal{F}$ is rigidly attached to an on-board camera (e.g., a camera mounted on a robot end-effector), the stationary coordinate frame $\mathcal{F}^*$ is attached to any arbitrary pose of the camera, and the coordinate frame $\mathcal{F}_t$ is attached to a stationary object. Without loss of generality, the frame $\mathcal{F}^*$ is considered to coincide with the initial pose of the on-board camera, i.e., $\mathcal{F}|_{t=t_0}$, and it is referred to as an auxiliary camera. The unit vectors along the x, y, and z coordinate axes of $\mathcal{F}$, $\mathcal{F}^*$, and $\mathcal{F}_t$ are denoted by $\{\hat{x}, \hat{y}, \hat{z}\}$, $\{\hat{x}^*, \hat{y}^*, \hat{z}^*\}$, and $\{\hat{x}_t, \hat{y}_t, \hat{z}_t\}$, respectively. The unit vector $\hat{z}$ along the z-axis of $\mathcal{F}$ is considered to coincide with the optical axis of the camera. The linear and the angular velocities of the camera expressed in $\mathcal{F}$ are

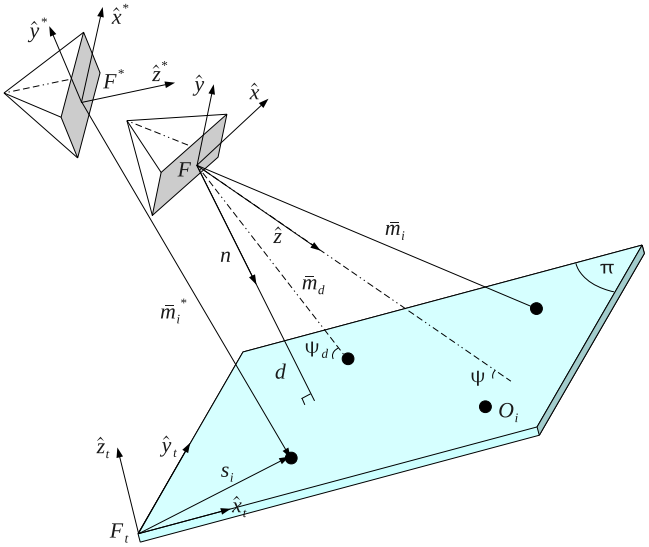

Fig. 2. Relationship between the coordinate frames $\mathcal{F}$, $\mathcal{F}^*$, and $\mathcal{F}_t$ attached to the current camera, the auxiliary camera, and the object, respectively.

denoted by $v_c(t) \in \mathbb{R}^3$ and $\omega_c(t) \in \mathbb{R}^3$, respectively. The object is represented in an image by four[2] feature points such that the corresponding Euclidean features, $\mathcal{O}_i$ $\forall i = 1, 2, 3, 4$, are coplanar and non-collinear. The plane defined by $\mathcal{O}_i$ is denoted as π, and the unknown Euclidean distance of $\mathcal{O}_i$ from the origin of $\mathcal{F}_t$ be $s_i \in \mathbb{R}^3$ $\forall i = 1, 2, 3, 4$ as shown in Fig. 2.

To relate the coordinate frames, let $R(t)$, $R^* \in \mathbb{SO}^3$ denote the rotation from $\mathcal{F}$ to $\mathcal{F}_t$ and $\mathcal{F}^*$ to $\mathcal{F}_t$, respectively, and the corresponding translation from $\mathcal{F}$ to $\mathcal{F}_t$ and $\mathcal{F}^*$ to $\mathcal{F}_t$ be denoted by $x_f(t)$, $x_f^* \in \mathbb{R}^3$, respectively. From the geometry between the camera coordinate frames and the object frame, as shown in Fig. 2, the following relationships can be developed:

$$\bar{m}_i = x_f + Rs_i, \qquad \bar{m}_i^* = x_f^* + R^* s_i \tag{1}$$

where $\bar{m}_i(t)$, $\bar{m}_i^* \in \mathbb{R}^3$ denote the Euclidean coordinates of the features points $\mathcal{O}_i$ expressed in $\mathcal{F}$ and $\mathcal{F}^*$, respectively, as

$$\bar{m}_i(t) \triangleq \begin{bmatrix} x_i(t) & y_i(t) & z_i(t) \end{bmatrix}^T, \tag{2}$$

$$\bar{m}_i^* \triangleq \begin{bmatrix} x_i^* & y_i^* & z_i^* \end{bmatrix}^T. \tag{3}$$

Assumption 1. In Eqs. (2) and (3), $z_i(t), z_i^* \geq \varepsilon_z$ for any constant $\varepsilon_z \in \mathbb{R}^+$. This is a physically motivated assumption that guarantees that an object is always in front of the camera.

Using the expressions in Eq. (1), the relationship between $\bar{m}_i(t)$ and $\bar{m}_i^*$ can be obtained as

$$\bar{m}_i^* = \bar{x}_f + \bar{R}\bar{m}_i \tag{4}$$

[2] Image analysis methods can be used to identify planar objects (e.g. using color, texture differences). These computer vision methods can be used to help determine and isolate four coplanar feature points. For the requirement of four coplanar and non-collinear feature points, the readers are encouraged to refer to [34].

where $\bar{R} = R^* R^T \in \mathbb{SO}^3$ and $\bar{x}_f = x_f^* - \bar{R} x_f \in \mathbb{R}^3$ denote the rotation and translation vectors, respectively, between $\mathcal{F}$ and $\mathcal{F}^*$. By using the projective relationship, $d = n^T \bar{m}_i$, the expression in Eq. (4) can be written as

$$\bar{m}_i^* = \left(\bar{R} + \frac{\bar{x}_f}{d} n^T \right) \bar{m}_i \tag{5}$$

where $d(t) > \varepsilon$ for some positive $\varepsilon \in \mathbb{R}$ denotes the depth, and $n(t) \in \mathbb{R}^3$ is the unit normal from $\mathcal{F}$ to the plane π as shown in Fig. 2. To facilitate the subsequent development, the normalized Euclidean coordinates of the feature points can be expressed in $\mathcal{F}$ and $\mathcal{F}^*$, denoted by $m_i(t)$, $m_i^* \in \mathbb{R}^3$, respectively, as follows:

$$m_i \triangleq \frac{\bar{m}_i}{z_i}, \qquad m_i^* \triangleq \frac{\bar{m}_i^*}{z_i^*}. \tag{6}$$

From the expressions in Eqs. (5) and (6), the rotation and translation between the coordinate frames $\mathcal{F}$ and $\mathcal{F}^*$ can now be related in terms of the normalized Euclidean coordinates of the features as

$$m_i^* = \underbrace{\left(\frac{z_i}{z_i^*} \right)}_{\alpha_i} \underbrace{\left(\bar{R} + x_h n^T \right)}_{H} m_i \tag{7}$$

where $\alpha_i(t) \in \mathbb{R}$ denotes the depth ratio, $H(t) \in \mathbb{R}^{3\times 3}$ denotes the Euclidean homography [35], and $x_h(t) \in \mathbb{R}^3$ denotes the scaled translation vector that is defined as $x_h = \bar{x}_f / d$.

Each Euclidean feature point $\mathcal{O}_i$ will have a projected pixel coordinate in the current and the auxiliary camera as

$$p_i \triangleq \begin{bmatrix} u_i & v_i & 1 \end{bmatrix}^T, \qquad p_i^* \triangleq \begin{bmatrix} u_i^* & v_i^* & 1 \end{bmatrix}^T \tag{8}$$

where $p_i(t)$, $p_i^* \in \mathbb{R}^3$ represent the pixel (i.e., image-space) coordinates of the feature points expressed in $\mathcal{F}$ and $\mathcal{F}^*$, respectively, and $u_i(t)$, $v_i(t)$, u_i^*, $v_i^* \in \mathbb{R}$.

To calculate the Euclidean homography given in Eq. (7) using the pixel information in Eq. (8), the projected pixel coordinates are related to the normalized Euclidean coordinates by a pin-hole camera model as

$$p_i = A m_i, \qquad p_i^* = A m_i^* \tag{9}$$

where $A \in \mathbb{R}^{3\times 3}$ is a known, constant, and globally invertible intrinsic camera calibration matrix of the form given in [21]. By substituting (9) into (7), the following relationship can be obtained:

$$p_i^* = \alpha_i \underbrace{\left(A H A^{-1} \right)}_{G} p_i \tag{10}$$

where $G(t) = [g_{ij}(t)] \in \mathbb{R}^{3\times 3}$ $\forall i, j = 1, 2, 3$ denotes a projective homography. The projective homography is defined up to a scalar multiple, i.e., $g_{33} = 1$. A set of eight linear equations can be developed from Eq. (10) using the four feature point correspondences to determine the eight unknowns in $G(t)$, and various techniques (e.g., see [34]) can be used to decompose the Euclidean homography, to obtain $\alpha_i(t)$, $n(t)$, $x_h(t)$, $\bar{R}(t)$.

In standard visual servo control problems, the relationship in Eq. (10) is obtained using feature points seen in the current image and an *a priori* acquired reference image corresponding

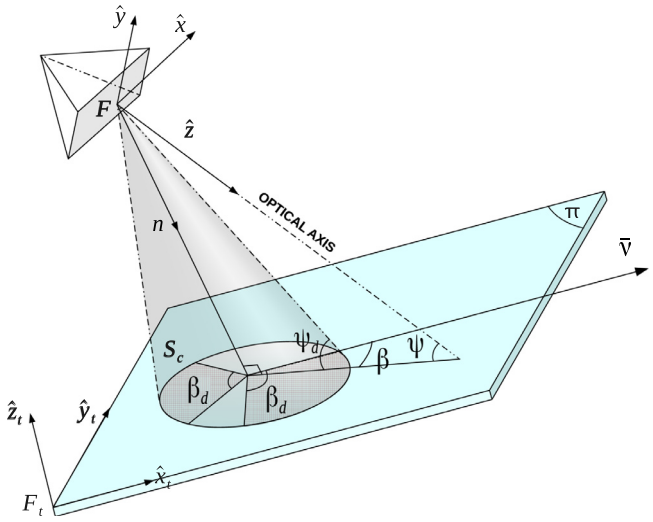

Fig. 3. The angle of obliquity $\psi(t)$ and the direction of arrival $\beta(t)$ of the camera along with the terminal angular constraints, ψ_d and β_d.

to a desired pose. The homography decomposition, as a result, provides the required rotation and translation components to regulate the camera from its current pose to the desired pose. In the absence of reference image, the feature points viewed by the auxiliary camera $\mathcal{F}^*$ do not provide meaningful rotation and translation information for regulation. However, the depth ratio $\alpha_i(t)$ and the unit normal $n(t)$ establish a weak relative pose between the camera $\mathcal{F}$ and the object $\mathcal{F}_t$. The relative pose in terms of $\alpha_i(t)$ and $n(t)$ is considered to be weak because these parameters cannot fully constrain the camera to yield a unique pose. Specifically, $\alpha_i(t)$ only provides the relative depth of the feature plane from $\mathcal{F}$, and $n(t)$ can only partially identify the orientation of $\mathcal{F}_t$ with respect to $\mathcal{F}$. Nevertheless, the subsequent development will exploit this weak relative pose information to formulate a new visual servo control approach that does not rely on a reference image.

3. Definitions

In the absence of a reference image, the presented visual servo controller uses terminal angular constraints to define the desired orientation of the camera. Motivated by practical examples, the following two new definitions are introduced to facilitate development of terminal constraints:

Definition 1 (Angle of Obliquity)**.** The *angle of obliquity* $\psi(t) \in (0, \pi/2]$ is defined as the angle made by the camera's optical axis with the feature point plane, i.e., the angle between the z-axis of frame $\mathcal{F}$ and the plane π as shown in Fig. 3.

Definition 2 (Direction of Arrival)**.** The *direction of arrival* $\beta(t) \in [0, 2\pi)$ is defined as the angle between a reference direction $\bar{v}$ (e.g., the local north) with respect to the object plane and the projection of the camera's optical axis on the object plane as shown in Fig. 3.

The terminal constraints are defined in terms of the desired angle of obliquity ψ_d and the desired direction of arrival β_d. The angle of obliquity constraint provides the desired angle of the camera's optical axis with respect to the feature plane, i.e., $\psi_d \in (0, \pi/2]$. The direction of arrival can be an angle or, in general, a range of possible angles. This is motivated by the fact that some applications may require the direction of arrival to not take certain values β_x (e.g., to avoid obstacles or being detected) while permitting the rest, i.e., $\beta_d = [0, 2\pi) \setminus \beta_x$. To this end, the direction of arrival constraint can be expressed as a union of $k \in \mathbb{N}$ pairwise disjoint closed intervals $\beta_d = [\underline{\beta_{d1}}, \overline{\beta_{d1}}] \cup [\underline{\beta_{d2}}, \overline{\beta_{d2}}] \cup \cdots \cup [\underline{\beta_{dk}}, \overline{\beta_{dk}}]$, where $0 \leq \underline{\beta_{d1}} \leq \overline{\beta_{d1}} < \underline{\beta_{d2}} \leq \overline{\beta_{d2}} < \cdots < \underline{\beta_{dk}} \leq \overline{\beta_{dk}} < 2\pi$. The "gaps" between these intervals represent the proscribed directions of arrival.

Corresponding to the desired angle of incidence, the optical axis of the camera can be represented by a pencil of lines intersecting the feature plane π at an angle ψ_d, describing generatrix lines of a right circular cone $\mathcal{S}_c$ as shown in Fig. 3. The apex of $\mathcal{S}_c$ coincides with the origin of $\mathcal{F}$ and the unit normal $n(t)$, defined in Eq. (5), coincides with the height of the cone, such that any orientation of $\mathcal{F}$ with its z-axis directed along any generatrix of the lateral surface will satisfy the desired angle of obliquity constraint. From the definition of β_d above, the direction of arrival can be a singleton, or it can be represented as a union of k closed intervals describing sectors of the base of the cone as shown by the hatched regions in Fig. 3. Consider the case when the direction of arrival is a singleton, i.e., $\beta_d \in [0, 2\pi)$. Then, β_d together with ψ_d obtain a generatrix along which the optical axis can be pointed to satisfy the constraints. However, it should be noted that the roll angle about the optical axis is not uniquely defined. When β_d is represented using k closed intervals, an infinitely large number of solutions (i.e., generatrix lines) can be obtained that satisfy β_d. Therefore, the challenge is to uniquely identify the desired orientation of $\mathcal{F}$ that will satisfy the terminal angular constraints. Since the optical axis is in the null-space of the rotation about z-axis, the roll angle about the optical axis does not affect ψ_d and β_d. Therefore, the objective of identifying the desired orientation of the camera reduces to obtaining a generatrix of $\mathcal{S}_c$ that satisfies the terminal constraints. A unique generatrix is obtained in Section 4.1 by posing a constrained optimization problem that minimizes camera motion.

4. Controller development

4.1. Rotation controller

The objective of the presented visual servo controller is to ensure that the camera is regulated to the object plane while satisfying the terminal angular constraints. Specifically, the orientation of $\mathcal{F}$ is regulated to an orientation defined by a desired angle of obliquity ψ_d and a desired direction of arrival β_d. Mathematically, the rotation control objective can be defined as

$$\psi(t) \to \psi_d \quad \forall \psi_d \in (0, \pi/2), \qquad \beta(t) \to \beta_d. \tag{11}$$

Remark 1. When the objective is to arrive normal to the plane, $\psi_d = \pi/2$, the generatrix lines coincide with the axis of $\mathcal{S}_c$, i.e., the cone reduces to a line perpendicular to the object plane along $n(t)$. Therefore, the desired orientation of the camera is such that the optical axis is directed along $n(t)$ (see Fig. 3). Further, since the cone reduces to a line, from Definition 2, β_d is not defined. Controller development for the singular case when $\psi_d = \pi/2$ will be presented in Section 4.1.1.

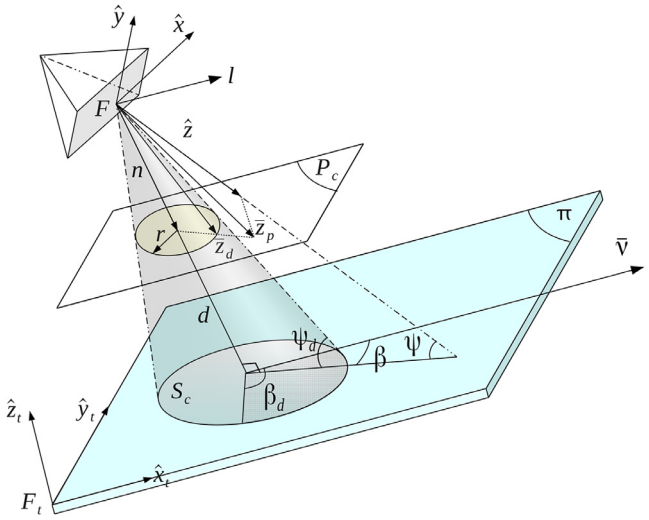

Fig. 4. Geometrical construction to identify the desired orientation of the optical axis that intersects feature plane π.

The objective, as stated in (11), is to intersect the plane π at the desired angle of incidence ψ_d and from the desired direction of arrival β_d. As discussed in Section 3, a desired generatrix can be obtained by minimizing the rotation between the optical axis and the generatrix lines that satisfy β_d. Subsequently, the rotation control objective can be satisfied by directing the optical axis along the desired generatrix.

The optimization problem can be stated as finding a generatrix, among all the generatrix lines that satisfy β_d, that is at a minimum distance from the unit vector $\hat{z}$ along the optical axis. Consider a plane $\mathcal{P}_c$ parallel to the base of the cone and at a unit height from the apex as shown in Fig. 4. The intersection of the generatrix with $\mathcal{P}_c$ describes a circle $\mathcal{C}$ centered at $n(t) \in \mathbb{R}^3$ and of radius $r = \cot \psi_d$.

Let $l(t) \in \mathbb{R}^3$ be the unit vector along the reference direction $\bar{\nu} \in \mathbb{R}^3$ measured in $\mathcal{F}$ and $m(t) \in \mathbb{R}^3$ be a unit vector, such that $\{l, m, n\}$ form the basis of a right-handed orthogonal coordinate frame with origin at the origin of $\mathcal{F}$. Now consider the projection of $\hat{z}$ onto the lm-plane, denoted by $z_{lm}(t) \in \mathbb{R}^3$, which can be obtained as $z_{lm} = \hat{z} - n\langle n, \hat{z}\rangle$, such that the angle between $z_{lm}(t)$ and $l(t)$, i.e., the direction of arrival, is $\beta = \cos^{-1}(\langle l, z_{lm}\rangle/|z_{lm}|)$ for $\beta(t) \in [0, 2\pi)$, where $\langle a, b\rangle$ indicates the inner product between a and b. Let $\phi \in [0, 2\pi)$ be the angle of rotation about n measured with respect to a vector that is rotated through $\pi + \beta$ with respect to l in the lm-plane, and $\phi'(t) \in [\pi + \beta, 3\pi + \beta)$ be defined as $\phi' \triangleq \pi + \phi + \beta$.

The circle $\mathcal{C}$ can then be parameterized in terms of $\phi'(t)$ as

$$\begin{aligned} p_c &= n + \cot \psi_d \big(\cos(\phi')l + \sin(\phi')m + 0n\big) \\ &= n + \cot \psi_d w(\phi') \end{aligned} \tag{12}$$

where $w(\phi') = \cos(\phi')l + \sin(\phi')m + 0n$, and the locus of points $p_c(\phi', t) \in \mathbb{R}^3$ measured in $\mathcal{F}$ for $\phi'(t) \in [\pi + \beta, 3\pi + \beta)$ for every fixed $t \geq 0$ define $\mathcal{C}$.

The squared distance $h(\phi', t) : [\pi + \beta, 3\pi + \beta) \times [0, \infty) \to \mathbb{R}^+$ from $\hat{z}$ to any point $p_c(\phi', t)$ of the circle can be written as

$$h = \langle (n - \hat{z}), (n - \hat{z})\rangle + \cot \psi_d^2 + 2\langle (n - \hat{z}), w\rangle \cot \psi_d. \tag{13}$$

The function $h(\phi', t)$ satisfies the following properties:

Property 1. *$H_t(\phi') := h(\phi', t)$ is a positive definite function of $\phi'(t)$ for every fixed $t \geq 0$, i.e., $H_t(\phi') > 0 \forall t$.*

Property 2. *$H_t(\phi')$ is a real-valued smooth function of $\phi'(t)$ for every fixed $t \geq 0$.*

Property 3. *$H_t(\phi')$ is a unimodular function of $\phi'(t)$ for every fixed $t \geq 0$ as there exists $\hat{\phi}' \in [a, b]$ for any $a < b$ and $[a, b] \subseteq [\pi + \beta, 3\pi + \beta)$ such that $H_t(\phi')$ is decreasing for $\phi' \in [a, \hat{\phi}']$ and increasing for $\phi' \in [\hat{\phi}', b]$. $H_t(\phi')$ has no local minima and exhibits a unique global minimum. The linear map $(\phi, \beta) \mapsto \phi'$ defined previously guarantees unimodularity of $H_t(\phi')$, and yields the global minimum at $\phi' = 2\pi + \beta$.*

If, for any fixed $t \geq 0$, $n(t) = \hat{z}$, i.e., the optical axis is directed normal to the object plane and $\psi_d \neq \pi/2$, then $H_t(\phi')$ is not unimodular. This is due to the fact that, for $n(t) = \hat{z}$, every point $P_t(\phi') := p_c(\phi', t)$ on $\mathcal{C}$ is equidistant from $\hat{z}$, which is directed towards the center of $\mathcal{C}$. Specifically, at $n(t) = \hat{z}$ and $\psi_d \neq \pi/2$, $H_t(\phi') = \cot \psi_d^2$ is a constant function. However, this degenerate case can be avoided by designing a controller that ensures $n(t) \neq \hat{z}$ when $\psi_d \neq \pi/2$ to preserve unimodularity of $H_t(\phi')$.

Property 4. *$h(\phi', t) \in \mathbb{R}$ is a continuously differentiable function of time. To prove, consider the time derivative of $h(\phi', t)$ as*

$$\frac{dh}{dt} = 2\left\langle (n - \hat{z}), \frac{dn}{dt} \right\rangle + 2\cot\psi_d \left\langle w, \frac{dn}{dt} \right\rangle + 2\cot\psi_d \left\langle (n - \hat{z}), \frac{dw}{dt} \right\rangle \tag{14}$$

where, using the definitions of $w(\phi')$ and $\phi'(t)$, $dw/dt = (d\beta/dt)(dw/d\phi')$. Further, $w(\phi')$ is a smooth function of $\phi'(t)$ for every fixed $t \geq 0$. For continuous linear and angular motion of the camera, the position and orientation of $\mathcal{F}$ with respect to any stationary coordinate frame is continuously differentiable. As a result, $\beta(t)$ is a continuously differentiable function. Further, it is clear from the kinematics of the unit vector, $\dot{n}(t) = -[\omega_c]_\times n(t)$, that $n(t)$ is a continuously differentiable vector field. Consequently, from Eq. (14), it is evident that dh/dt exists and is continuous in $\mathbb{R}$. Example: Fig. 5 shows the distance $h(\phi', t)$ of an arbitrarily moving point from a circle in $\mathbb{R}^3$.

The direction of arrival constraint β_d can be mapped to $\phi'_d \subseteq [\pi + \beta, 3\pi + \beta)$. Consider the general scenario when β_d is given by a union of k closed intervals as $\beta_d = [\underline{\beta_{d1}}, \overline{\beta_{d1}}] \cup [\underline{\beta_{d2}}, \overline{\beta_{d2}}] \cup \cdots \cup [\underline{\beta_{dk}}, \overline{\beta_{dk}}]$ as discussed in Section 3. Let $j = 1, 2, \ldots, k$ denote the k intervals, and let the intervals be written as $[\underline{\beta_{dj}}, \overline{\beta_{dj}}]$. Corresponding to these k intervals, let $[\underline{\phi'_{dq}}, \overline{\phi'_{dq}}]$ for $q = 1, 2, \ldots, k'$ be the intervals that are mapped to $[\pi + \beta, 3\pi + \beta)$, which can be obtained as

$$\begin{aligned}
&\left[\underline{\phi'_{dq}}, \overline{\phi'_{dq}}\right] = \left[2\pi + \underline{\beta_{dj}}, 2\pi + \overline{\beta_{dj}}\right] \quad \text{if} \quad 0 \leq \underline{\beta_{dj}} \leq \overline{\beta_{dj}} < \pi + \beta \\
&\left[\underline{\phi'_{dq}}, \overline{\phi'_{dq}}\right] = \left[2\pi + \underline{\beta_{dj}}, 3\pi + \beta\right) \Big\} \quad \text{if} \quad 0 \leq \underline{\beta_{dj}} < \pi + \beta \text{ and} \\
&\left[\underline{\phi'_{dq+1}}, \overline{\phi'_{dq+1}}\right] = \left[\pi + \beta, \overline{\beta_{dj}}\right] \qquad \pi + \beta \leq \overline{\beta_{dj}} < 2\pi \\
&\left[\underline{\phi'_{dq}}, \overline{\phi'_{dq}}\right] = \left[\underline{\beta_{dj}}, \overline{\beta_{dj}}\right] \quad \text{if} \quad \pi + \beta \leq \underline{\beta_{dj}} \leq \overline{\beta_{dj}} < 2\pi.
\end{aligned} \tag{15}$$

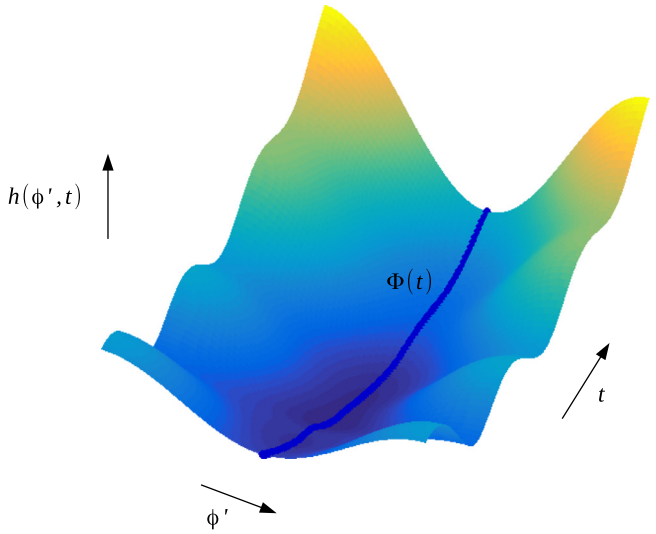

Fig. 5. Plot showing distance $h(\phi', t)$ of an arbitrarily moving point from a circle in $\mathbb{R}^3$, and the minimum distance $\Phi(t)$ as a function of time when $\beta_d = [0, 2\pi)$.

It can be seen from Eq. (15) that any interval $[\underline{\beta_{dj}}, \overline{\beta_{dj}}]$ such that $0 \leq \underline{\beta_{dj}} < \pi + \beta$ and $\pi + \beta \leq \overline{\beta_{dj}} < 2\pi$ yields two disjoint sets of ϕ'_d. Therefore, the set ϕ'_d contains equal or more number of closed intervals as β_d, i.e., $\phi'_d = [\underline{\phi'_{d1}}, \overline{\phi'_{d1}}] \cup [\underline{\phi'_{d2}}, \overline{\phi'_{d2}}] \cup \cdots \cup [\underline{\phi'_{dk'}}, \overline{\phi'_{dk'}}]$, where $k' \geq k$.

Remark 2. Using Eq. (15) and the fact that β_d can be given as a union of k closed intervals, ϕ'_d will be comprised of at least k pairwise disjoint sets. Since $H_t(\phi')$ is a unimodular function over $\phi' \in [\pi + \beta, 3\pi + \beta)$ (Property 3), it is guaranteed that $H_t(\phi' \in \phi'_d)$ is unimodular on each of its k' disjoint sets.

Recall that the objective is to obtain a generatrix of $\mathcal{S}_c$ that is at minimum distance from $\hat{z}$ and satisfies the desired direction of arrival constraint $\beta \in \beta_d$. Based on Eq. (13), the problem can be seen as finding a point on $\mathcal{C}$ for which $H_t(\phi' \in \phi'_d)$ is minimized for every fixed $t \geq 0$. Mathematically, it can be stated as

$$\Phi(t) := \arg \min_{\phi' \in \phi'_d} H_t(\phi') \tag{16}$$

where $\Phi(t) \in [\pi + \beta, 3\pi + \beta)$ is the value of $\phi'(t)$ at which the function $H_t(\phi')$ attains its minimum value for $\phi' \in \phi'_d$ for every fixed $t \geq 0$ as shown in Fig. 5.

Algorithm. This section describes an algorithmic approach to obtain an optimal solution of Eq. (16). The following scenarios are considered based on β_d.

1. When there is no restriction on the direction of arrival, i.e., $\beta_d = [0, 2\pi)$, ϕ'_d takes every value in its domain $\phi'_d \in [\pi + \beta, 3\pi + \beta)$. Therefore, Eq. (16) can be considered as an unconstrained optimization problem for which Property 3 shows that the global minimum exists at $\Phi = 2\pi + \beta$.

2. Consider the scenario when β_d is a singleton, i.e., $\beta_d \in [0, 2\pi)$. Hence, ϕ'_d is also a singleton and can be obtained using Eq. (15). Based on the constraint $\phi' \in \phi'_d$, it is clear that the set of feasible solutions trivially reduces to a singleton, *viz.* $\phi' = \phi'_d$. Since $H_t(\phi')$ is evaluated at a single value of its argument (i.e., ϕ'_d), it may not be regarded as the minimum solution. However, $\phi' = \phi'_d$ provides the orientation of the camera that satisfies the desired direction of arrival. Therefore, with slight abuse of notation, let the solution be written as $\Phi = \phi'_d$ to facilitate subsequent development.
3. Consider the scenario when $\beta_d = [\underline{\beta_{d1}}, \overline{\beta_{d1}}] \cup [\underline{\beta_{d2}}, \overline{\beta_{d2}}] \cup \cdots \cup [\underline{\beta_{dk}}, \overline{\beta_{dk}}]$. The following two cases exist based on the present direction of arrival $\beta(t)$ with respect to β_d.
   (a) ($\beta \in \beta_d$) The solution of the unconstrained optimization problem in scenario 1 shows that the global minimum exists at $2\pi + \beta$. Hence, although $\beta_d \neq [0, 2\pi)$, if $\beta \in \beta_d$, then using Remark 2 and Property 3 it can be shown that the solution of Eq. (16) nevertheless remains at $\Phi = 2\pi + \beta$.
   (b) ($\beta \notin \beta_d$) If $\beta \notin \beta_d$ then we seek a solution closest to $2\pi + \beta$ that satisfies the constraint $\phi' \in \phi'_d$. Let $j^* \in [1, k']$ be an interval of ϕ'_d that is closest to $2\pi + \beta$, which can be identified as

$$j^* = \arg\min_j \Big(\min \Big(|2\pi + \beta - \underline{\phi'_{dj}}|, |2\pi + \beta - \overline{\phi'_{dj}}| \Big) \Big). \tag{17}$$

   Therefore, based on Remark 2, the solution of Eq. (16) can be obtained as

$$\Phi = \begin{cases} \overline{\phi'_{dj^*}} & \text{if } \underline{\phi'_{dj^*}} < 2\pi + \beta \\ \underline{\phi'_{dj^*}} & \text{if } \underline{\phi'_{dj^*}} > 2\pi + \beta \end{cases} \tag{18}$$

Property 5. *When β_d is comprised of k' disjoint sets, using Properties 3 and 4, it can be concluded that $\Phi(t)$ is a piecewise continuously differentiable function of t. Specifically, the trajectory of $\Phi(t)$ is continuously differentiable within each of the k' sets and exhibits a jump discontinuity at time $t' > 0$ if and only if the optimal solution $\Phi(t')$ falls in another set.*

When β_d is unconstrained, $\beta_d = [0, 2\pi)$, $\Phi(t)$ is a continuously differentiable function of t. Also, when β_d is singleton, $\beta_d \in [0, 2\pi)$, $\Phi(t)$ is a continuously differentiable function of t.

Let $\bar{z}_d(t) \in \mathbb{R}^3$ be a vector along the generatrix of $\mathcal{S}_c$ corresponding to the optimal solution $\Phi(t)$ in Eq. (16) as shown in Fig. 4. Using the expression in Eq. (12), $\bar{z}_d(t)$ can be obtained as

$$\bar{z}_d = n + \cot\psi_d w(\Phi) \tag{19}$$

such that $\bar{z}_d$ is at the minimum angular distance from $\hat{z}$, and when the optical axis is directed along $\bar{z}_d$, the camera satisfies $\psi = \psi_d$ and $\beta \in \beta_d$ constraints.

Remark 3. Consider the case when the direction of arrival is unconstrained, i.e., $\beta_d = [0, 2\pi)$. Taking the derivative of Eq. (13) with respect to $\phi'(t)$, the following expression can be obtained:

$$\frac{dh}{d\phi'} = 2\left\langle (n - \hat{z}), \frac{dw}{d\phi'} \right\rangle \cot\psi_d. \tag{20}$$

From the definition of $w(\phi')$ in Eq. (12), we get $w \cdot dw/d\phi' = 0$. Since $n \cdot w = 0$, it can be shown that w is parallel to the projection of $(\hat{z} - n)$ onto the plane $\mathcal{P}_c := \langle n, (p_c - n) \rangle$, where $p_c(\phi', t)$ is defined in Eq. (12). Therefore, the closed form expression for $\bar{z}_d(t)$ in

Eq. (19) can be obtained as

$$\bar{z}_d = n + \cot\psi_d \frac{\bar{z}_p - n}{|\bar{z}_p - n|} \tag{21}$$

where $\bar{z}_p(t) \in \mathbb{R}^3$ is the projection of $\hat{z}$ onto the plane $\mathcal{P}_c$ as shown in Fig. 4. The vector $(\bar{z}_p - n)$ in Eq. (21) can be obtained as

$$\bar{z}_p - n = \hat{z} - n - \langle n, (\hat{z} - n)\rangle n. \tag{22}$$

For $\beta_d = [0, 2\pi)$, the expressions in Eqs. (21) and (22) provide the desired orientation of the camera without the knowledge of its direction of arrival $\beta(t)$.

As stated previously, the rotation control objective is to regulate the orientation of the camera coordinate frame $\mathcal{F}$ such that the optical axis (z-axis) is along $\bar{z}_d(t)$, i.e., along the desired generatrix. To quantify the angular mismatch between $\hat{z}$ and a unit vector, say $\hat{z}_d(t)$, along $\bar{z}_d(t)$, a rotation error-like signal, denoted by $e_\omega(t) \in \mathbb{R}^3$, is defined by the angle axis representation as

$$e_\omega \triangleq u\theta = \begin{bmatrix} e_{\omega x} & e_{\omega y} & e_{\omega z} \end{bmatrix}^T \tag{23}$$

where $e_{\omega x}(t)$, $e_{\omega y}(t)$, $e_{\omega z}(t) \in \mathbb{R}$ are the components of $e_\omega(t)$ about the x, y, and z-axis, respectively. In Eq. (23), $u(t) \in \mathbb{R}^3$ represents a unit axis of rotation such that $u = \hat{z} \wedge \hat{z}_d$, and $\theta(t) = \cos^{-1}\langle \hat{z}, \hat{z}_d \rangle \in \mathbb{R}$ denotes the rotation angle about $u(t)$ that is confined to $0 \leq \theta(t) < 2\pi$ (see [9]). Taking the time derivative of Eq. (23), the open-loop error dynamics for $e_\omega(t)$ can be expressed as

$$\dot{e}_\omega = -L_\omega \omega_c \tag{24}$$

where $L_\omega(t) \in \mathbb{R}^{3\times 3}$ is defined as

$$L_\omega \triangleq I_3 - \frac{\theta}{2}[u]_\times + \left(1 - \frac{\operatorname{sinc}(\theta)}{\operatorname{sinc}^2(\frac{\theta}{2})}\right)[u]_\times^2. \tag{25}$$

In Eq. (25), the $\operatorname{sinc}(\theta)$ term denotes the unnormalized sinc function. At $\theta(t) = 2\pi$, it can be seen that the determinant of L_ω is singular, and L_ω^{-1} does not exist. Given the open-loop rotation error dynamics in Eq. (24) and the subsequent stability analysis, the control input $\omega_c(t)$ can be designed as

$$\omega_c = \Lambda_\omega \operatorname{diag}(|e_\omega|^\alpha) \operatorname{sgn}(e_\omega) \tag{26}$$

where $\Lambda_\omega \in \mathbb{R}_{>0}$ is the known constant control gain, $\operatorname{diag}(\cdot)$ denotes a diagonal matrix, $\operatorname{sgn}(\cdot)$ is a signum function, and $\alpha \in \mathbb{R}$ is a known constant such that $\alpha \in (0, 1)$. It must be pointed out that even in the presence of the discontinuous term $\operatorname{sgn}(e_\omega)$ the angular velocity control input $\omega_c(t)$ in Eq. (26) is a continuous function of time [36]. Substituting (26) into (24) gives the expression for the closed-loop error dynamics as

$$\dot{e}_\omega = -L_\omega \Lambda_\omega \operatorname{diag}(|e_\omega|^\alpha) \operatorname{sgn}(e_\omega). \tag{27}$$

Theorem 1. *The rotation controller in Eq. (26) guarantees that the orientation of the camera coordinate frame $\mathcal{F}$ is regulated to a desired orientation defined by ψ_d and β_d such that the origin is a practically globally finite-time-stable equilibrium for the closed-loop system in Eq. (27).*

Proof. Consider a positive definite Lyapunov candidate function $V_\omega(e_\omega)$ as

$$V_\omega = \frac{1}{2} e_\omega^T e_\omega. \tag{28}$$

After taking the time-derivative of Eq. (28) and substituting Eq. (27) in the resulting expression, the Lyapunov derivative can be obtained as

$$\dot{V}_\omega = -e_\omega^T \Lambda_\omega \text{diag}(|e_\omega|^\alpha)\text{sgn}(e_\omega) \tag{29}$$

where the fact that $e_\omega^T L_\omega = e_\omega^T$ is utilized. $e_\omega^T(t)$ can also be written as $e_\omega^T = \text{sgn}(e_\omega^T)\text{diag}(|e_\omega|)$. Therefore, the expression in Eq. (29) becomes

$$\dot{V}_\omega = -\text{sgn}(e_\omega^T)\Big[\Lambda_\omega \text{diag}(|e_\omega|)\text{diag}(|e_\omega|^\alpha)\Big]\text{sgn}(e_\omega). \tag{30}$$

It can be observed that the bracketed quantity in Eq. (30) is a positive definite symmetric diagonal matrix. As a result, the Lyapunov derivative can be expressed as

$$\dot{V}_\omega = -\text{sgn}(|e_\omega^T|)\Big[\Lambda_\omega \text{diag}(|e_\omega|)\text{diag}(|e_\omega|^\alpha)\Big]\text{sgn}(|e_\omega|) \tag{31}$$

$$= -\Lambda_\omega \|e_\omega\|^{\alpha+1} = -\Lambda_\omega (2V_\omega)^\mu \tag{32}$$

where $\|\cdot\|^p$ denotes the p-norm, and $\mu = (\alpha+1)/2$. It can be seen that the Lyapunov derivative in Eq. (32) is negative definite, $\dot{V}_\omega(e_\omega) < 0$. Based on $V_\omega(e_\omega) > 0$ and $\dot{V}_\omega(e_\omega) < 0$, it can be concluded that $e_\omega(t) \in \mathcal{L}_\infty$ and $e_\omega(t) \in \mathcal{L}_2$. Based on the fact that $e_\omega(t) \in \mathcal{L}_\infty$, Eqs. (23), (24), (26) and (27) can be used to prove that $u(t), \theta(t), L_\omega(t), \omega_c(t), \dot{e}_\omega(t) \in \mathcal{L}_\infty$. Using $\dot{e}_\omega(t) \in \mathcal{L}_\infty$ and Eq. (23), it is clear that $\dot{u}(t), \dot{\theta}(t) \in \mathcal{L}_\infty$. Taking the time derivative of Eq. (27) and using the above arguments, it can be shown that $\ddot{e}_\omega(t) \in \mathcal{L}_\infty$. Additionally, with $\Lambda_\omega > 0$ and $\alpha \in (0, 1)$, the rotation controller in Eq. (26) is continuous everywhere and locally Lipschitz everywhere except at the origin. Thus, according to Theorem 1 in [37], the origin is a practically globally finite-time-stable equilibrium of the closed-loop system in Eq. (27). The term practically global is used in lieu of global since the result is not valid for the singular point $\theta = 2\pi$ associated with the angle of rotation [14]. The upper bound on the convergence time for $e_\omega(0) \to 0$ can be obtained as [37]

$$t_\omega(e_\omega(0)) \leq \frac{1}{\Lambda_\omega 2^\mu (1-\mu)} V_\omega(e_\omega(0))^{1-\mu} = t'_\omega \tag{33}$$

where $t'_\omega \in \mathbb{R}_{>0}$. Hence, the developed rotation controller guarantees that the orientation of the camera is regulated to the desired orientation defined by ψ_d and β_d in finite time. □

4.1.1. Singular Case $\psi_d = \pi/2$

As stated in Remark 1, the control objective of $\psi_d = \pi/2$ can be satisfied by directing the optical axis along $n(t)$ normal to π. However, β_d is not defined since the cone $\mathcal{S}_c$ in Fig. 3 reduces to a line along $n(t)$. Further, p_c in Eq. (12) becomes a single point at $n(t)$, independent of $\phi'(t)$ or $\beta(t)$. Therefore, for this singular case, the rotation control objective is defined only in terms of the angle of obliquity as $\psi \to \psi_d = \pi/2$ or, equivalently, $\hat{z} \to n(t)$.

When $\psi_d = \pi/2$, the rotation error $e_\omega(t)$ can be expressed as the angular mismatch between $\hat{z}$ and $n(t)$ as $e_\omega = u\theta$, where $u = \hat{z} \wedge n$, and $\theta = \cos^{-1}\langle \hat{z}, n \rangle$. The design of the rotation controller in Eq. (26) and the subsequent stability analysis remains unchanged.

4.2. Translation controller

The controller in this paper is motivated by applications, such as autonomous grasping, where the objective for the camera is to reach the object. Therefore, the translation control objective is to ensure that the camera is regulated to the object plane. Specifically, the position of the origin of $\mathcal{F}$ is regulated to a desired feature $\mathcal{O}_i$, for any i. To develop the translation controller, a single feature point can be utilized. Without loss of generality, the subsequent development will be based on the feature $\mathcal{O}_1$, and hence, the subscript 1 will be utilized in lieu of i. Mathematically, the pixel coordinates $p_1(t)$ of $\mathcal{O}_1$ are regulated to the principal point or image center $p_d \triangleq \begin{bmatrix} 0 & 0 & 1 \end{bmatrix}^T$ as the camera approaches π in the sense that

$$p_1(t) \to \begin{bmatrix} 0 & 0 & 1 \end{bmatrix}^T, \qquad z_1(t) \to 0. \tag{34}$$

Remark 4. Although the objective to regulate the camera to the object plane (i.e., $z_1(t) \to 0$) violates Assumption 1, in practice the camera frame $\mathcal{F}$ intercepts π for some set $z_1 \in [z_{\min}, z_{\max}]$, where $z_{\max} \geq z_{\min} > \varepsilon_z$ [38,39]. This is due to the fact that the exact intercept value depends on the relative position of the camera with respect to the system (e.g., robotic arm, missile, aircraft) on which it is mounted, which can be obtained by coordinate transformation using the camera's extrinsic calibration parameters [21]. As a result, the Assumption 1 holds and singularity due to $z(t) = 0$ is avoided.

Let $p_{e1}(t) \in \mathbb{R}^3$ denote the extended image coordinates of $\mathcal{O}_1$ as

$$p_{e1} \triangleq \begin{bmatrix} u_1 & v_1 & \alpha_1 \end{bmatrix}^T \tag{35}$$

where $\alpha_1(t) \in \mathbb{R}$ is the depth ratio defined in Eq. (7). Also, let $p_{ed} \in \mathbb{R}^3$ denote the constant extended image coordinates of the desired image point as $p_{ed} = \mathbf{0}_{3\times 1}$, where $\mathbf{0}_{3\times 1}$ is a zero matrix.

The translation error $e_v(t) \in \mathbb{R}^3$ can be defined as the difference between $p_{e1}(t)$ and p_{ed} as

$$e_v \triangleq p_{e1} - p_{de} = \begin{bmatrix} e_{vx} & e_{vy} & e_{vz} \end{bmatrix}^T \tag{36}$$

where $e_{vx}(t)$, $e_{vy}(t)$, $e_{vz}(t) \in \mathbb{R}$ are the components of $e_v(t)$ along the x, y, and z-axis, respectively. It can be seen from Eq. (36) that when $e_v(t) \to 0$ the feature point $\mathcal{O}_1$ is regulated to the image center, and the depth of the camera is regulated such that $\alpha_1(t) \to 0$, i.e., $z_1(t) \to 0$.

Remark 5. Due to the absence of a reference image, the desired depth of the camera can only be defined relative to the auxiliary camera $\mathcal{F}^*$. Let $e_{vz}(t)$ in Eq. (36) be defined as $e_{vz} \triangleq \alpha_1 - \alpha_d$, where $\alpha_d = z_d/z_1^*$ is the desired depth ratio, and $z_d > 0$ is the constant depth of $\mathcal{O}_1$ corresponding to the desired pose of the camera. However, since z_1^* is unknown, α_d cannot be obtained to regulate the camera to the desired depth z_d. Any arbitrarily selected α_d can only regulate the camera to a relative depth with respect to the auxiliary camera. The exception being the case presented in this paper, where $z_d = 0$. This implies that, independent of the knowledge of z_1^*, $\alpha_d = 0$. Hence, the camera can be regulated to an absolute desired position on the plane π without the knowledge of z_1^* or reference image. Alternatively, if z_1^* is known or measurable, e.g., using stereo-vision or range identification methods [40–42], then α_d can be defined for the given z_d. The knowledge of z_1^* can thus enable the camera to be positioned at any desired depth $z_d > 0$.

Taking time-derivative of Eq. (36) and using $\dot{\bar{m}}_1 = -v_c + [\bar{m}_1]_\times \omega_c$, the open-loop error system can be developed as

$$z_1^* \dot{e}_v = \frac{1}{\alpha_1} L_v v_c + z_1^* L_{v\omega} \omega_c \tag{37}$$

where $L_v(t), L_{v\omega}(t) \in \mathbb{R}^{3\times 3}$ are defined as

$$L_v \triangleq \begin{bmatrix} -a_{1,1} & -a_{1,2} & a_{1,1}f + a_{1,2}g \\ 0 & -a_{2,2} & a_{2,2}g \\ 0 & 0 & -\alpha_1 \end{bmatrix}, \tag{38}$$

$$L_{v\omega} \triangleq \begin{bmatrix} a_{1,1}fg + a_{1,2} + a_{1,2}g^2 & -a_{1,1} - a_{1,1}f^2 - a_{1,2}fg & a_{1,1}g - a_{1,2}f \\ a_{2,2} + a_{2,2}g^2 & -a_{2,2}fg & -a_{2,2}f \\ -\alpha_1 g & \alpha_1 f & 0 \end{bmatrix}. \tag{39}$$

In Eq. (39), $f(u_1, v_1)$ and $g(v_1)$ are the auxiliary functions of the image coordinates as below

$$f = \frac{1}{a_{1,1}}\left[u_1 - \frac{a_{1,2}}{a_{2,2}}(v_1 - a_{2,3}) - a_{1,3}\right], \quad g = \frac{1}{a_{2,2}}\left[v_1 - a_{2,3}\right] \tag{40}$$

where $a_{i,j} \in \mathbb{R}\ \forall i, j = 1, 2, 3$ represents the known element from the camera calibration matrix A.

Based on the open-loop error system in Eq. (37), the linear velocity control input can be designed as

$$v_c = -\alpha_1 L_v^{-1}\left(\Lambda_v \mathrm{diag}(|e_v|^\gamma)\mathrm{sgn}(e_v) + \hat{z}_1^* L_{v\omega}\omega_c\right) \tag{41}$$

where $\Lambda_v \in \mathbb{R}^{3\times 3}$ is the positive definite symmetric diagonal matrix of control gain, $\gamma \in \mathbb{R}$ is a known constant such that $\gamma \in (0, 1)$, $\omega_c(t) \in \mathbb{R}^3$ is defined in Eq. (26), and the time-varying estimate $\hat{z}_1^*(t) \in \mathbb{R}$ of the unknown constant depth z_1^* is obtained using the direct adaptive update law as

$$\dot{\hat{z}}_1^* = \Gamma e_v^T L_{v\omega}\omega_c \tag{42}$$

where $\Gamma \in \mathbb{R}_{>0}$ is a known constant gain. Again, it is should be noted that the translation velocity control input $v_c(t)$ in Eq. (41) is a continuous function of time [36]. Substituting (41) into (37) the closed-loop system can be obtained as

$$z_1^* \dot{e}_v = -\Lambda_v \mathrm{diag}(|e_v|^\gamma)\mathrm{sgn}(e_v) + \tilde{z}_1^* L_{v\omega}\omega_c \tag{43}$$

where $\tilde{z}_1^*(t) \in \mathbb{R}$ is the parameter estimation error defined as

$$\tilde{z}_1^* \triangleq z_1^* - \hat{z}_1^*. \tag{44}$$

Theorem 2. *The translation controller in Eqs. (41) and (42) ensures that the position of the camera coordinate frame $\mathcal{F}$ is regulated to the desired position defined by $p_1(t) \to p_d$ and $z_1(t) \to 0$ such that the origin is a practically globally finite-time-stable equilibrium for the closed-loop system in Eq. (43).*

Proof. Consider a positive definite Lyapunov candidate function $V_{v1}(e_v, \tilde{z}_1^*)$ as

$$V_{v1} = \frac{1}{2} e_v^T z_1^* e_v + \frac{1}{2}\Gamma^{-1}\tilde{z}_1^{*2}. \tag{45}$$

Taking time derivative of Eq. (45) and substituting the closed-loop system Eq. (43) into the resulting expression, the Lyapunov derivative can be obtained as

$$\dot{V}_{v1} = -\Lambda_v e_v^T \text{diag}(|e_v|^\gamma)\text{sgn}(e_v) + e_v^T \tilde{z}_1^* L_{v\omega}\omega_c + \Gamma^{-1}\tilde{z}_1^*\dot{\tilde{z}}_1^*. \tag{46}$$

Using the time derivative of Eq. (44) and substituting (42), the Lyapunov derivative in Eq. (46) can be simplified as

$$\dot{V}_{v1} = -\Lambda_v e_v^T \text{diag}(|e_v|^\gamma)\text{sgn}(e_v). \tag{47}$$

Writing $e_v^T(t)$ as $e_v^T = \text{sgn}(e_v^T)\text{diag}(|e_v|)$, the Lyapunov derivative can be reduced to

$$\dot{V}_{v1} = -\text{sgn}(e_v^T)\Big[\Lambda_v \text{diag}(|e_v|)\text{diag}(|e_v|^\gamma)\Big]\text{sgn}(e_v) \tag{48}$$

where the bracketed quantity can be observed to be a positive definite symmetric diagonal matrix. As a result, the Lyapunov derivative becomes

$$\dot{V}_{v1} = -\text{sgn}(|e_v^T|)\Big[\Lambda_v \text{diag}(|e_v|)\text{diag}(|e_v|^\gamma)\Big]\text{sgn}(|e_v|) < 0. \tag{49}$$

Based on $V_{v1}(e_v, \tilde{z}_1^*) > 0$ and $\dot{V}_{v1}(e_v, \tilde{z}_1^*) < 0$, it can be concluded that $e_v(t)$, $\tilde{z}_1^*(t) \in \mathcal{L}_\infty$ and $e_v(t) \in \mathcal{L}_2$. Using Eq. (44) and the facts that z_1^*, $\tilde{z}_1^*(t) \in \mathcal{L}_\infty$, it can be shown that $\hat{z}_1^*(t) \in \mathcal{L}_\infty$. In addition, since $e_v(t), \omega_c(t) \in \mathcal{L}_\infty$, the expressions in Eqs. (36), (38), (39), (40), and (43) can be used to show that $L_v, L_{v\omega}, \dot{e}_v(t) \in \mathcal{L}_\infty$. Using the aforementioned arguments and the bounded inverse theorem, it can be concluded that the control input is bounded, $v_c(t) \in \mathcal{L}_\infty$. Based on the facts that $e_v(t), \dot{e}_v(t) \in \mathcal{L}_\infty$ and $e_v(t) \in \mathcal{L}_2$, Barbalat's Lemma can be evoked to prove that $\lim_{t\to\infty} e_v(t) \to 0$.

Further, in Theorem 1, it is proved that the rotation controller guarantees that $e_\omega \to 0$ in finite time $t(e_\omega(0))$ with an upper bound t'_ω as obtained in Eq. (33). From Eq. (26), it is clear that $\omega_c(t) \to 0$ as $e_\omega \to 0$. Therefore, after at most $t = t'_\omega$ time, the closed-loop error system in Eq. (43) reduces to

$$z_1^* \dot{e}_v = -\Lambda_v \text{diag}(|e_v|^\gamma)\text{sgn}(e_v) \qquad \forall t \in [t'_\omega, \infty). \tag{50}$$

To prove that the closed-loop system in Eq. (50) is finite-time-stable over $t \in [t'_\omega, \infty)$, consider a positive definite Lyapunov candidate function $V_{v2}(e_v) = e_v^T z_1^* e_v/2$. Taking time-derivative of $V_{v2}(e_v)$ and after substituting (50) and simplifying, the Lyapunov derivative can be obtained as $\dot{V}_{v2} = -\Lambda_v(2V_{v2})^\nu$, where $\nu = (\gamma+1)/2$. Using similar arguments as in Theorem 1, it can be proved that the origin is a practically globally finite-time-stable equilibrium of the closed-loop system in Eq. (50) over $t \in [t'_\omega, \infty)$. The term practically global is used in lieu of global since the result is not valid for non-positive depths of the objects, $z(t) \leq 0$ [14]. The upper bound on the convergence time for $e_v(t'_\omega) \to 0$ can be obtained as

$$t(e_v(t'_\omega)) \leq \frac{1}{\Lambda_v 2^\nu (1-\nu)} V_{v2}(e_v(t'_\omega))^{1-\nu} = t'_v \tag{51}$$

where $t'_v \in \mathbb{R}_{>0}$. From Eqs. (33) and (51), the bound on the time for $e_v(0) \to 0$ can therefore be obtained as $t(e_v(0)) \leq t'_\omega + t'_v$. Hence, the developed translation controller guarantees that the position of the camera is regulated to the desired position in finite time. □

5. Simulation results

A numerical simulation was performed to demonstrate the performance of the proposed visual servo controller. With the objective of arriving at the object plane with the desired angle

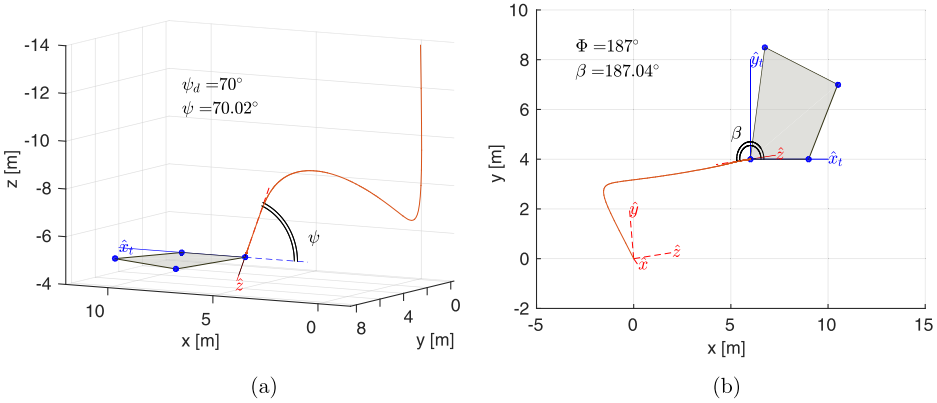

Fig. 6. Trajectory of the camera in the (a) 3D Euclidean space and (b) its projection on the xy-plane showing the achieved the angle of obliquity ψ and the direction of arrival β. The desired angle of obliquity is $\psi_d = 70^\circ$, the desired direction of arrival β_d is unconstrained, i.e., $\beta_d = [0, 2\pi)$, and the optimal direction of arrival solution is obtained as $\Phi = 187^\circ$. The Euclidean features on the stationary object are shown as blue (●). (For interpretation of the references to color in this figure legend, the reader is referred to the web version of this article.)

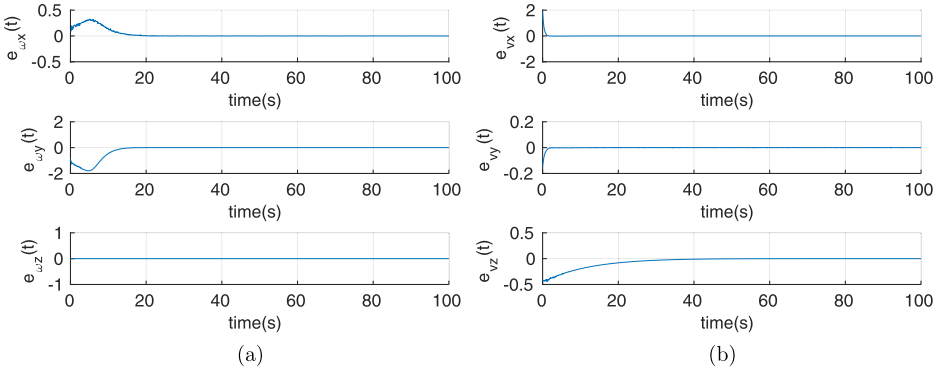

Fig. 7. (a) Rotation error $e_\omega(t)$ and (b) translation error $e_v(t)$ for terminal constraints $\psi_d = 70^\circ$ and $\beta_d = [0, 2\pi)$.

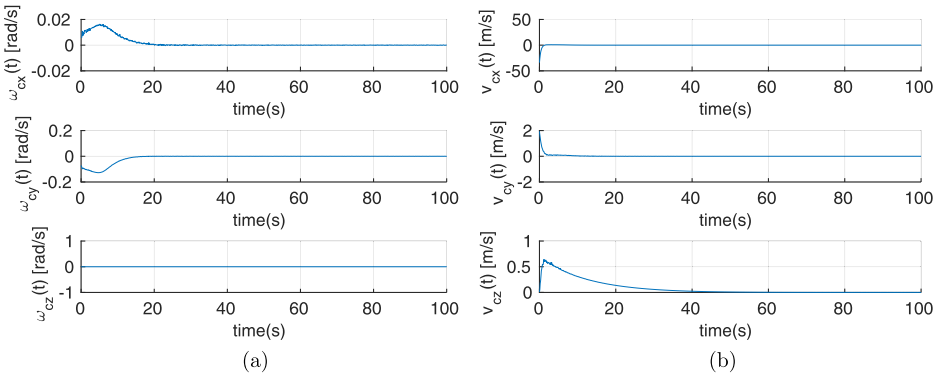

Fig. 8. (a) Angular velocity $\omega_c(t)$ and (b) linear velocity $v_c(t)$ of the camera for terminal constraints $\psi_d = 70^\circ$ and $\beta_d = [0, 2\pi)$.

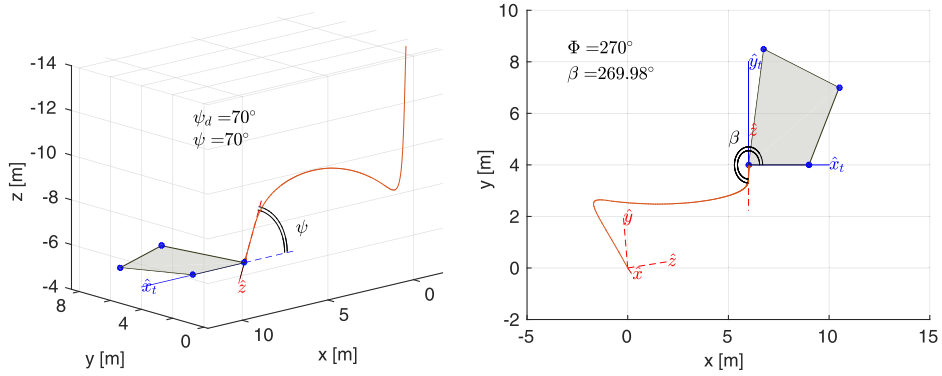

Fig. 9. Trajectory of the camera in the (a) 3D Euclidean space and (b) its projection on the *xy*-plane showing the achieved the angle of obliquity ψ and the direction of arrival β. The desired angle of obliquity is $\psi_d = 70°$, the desired direction of arrival β_d is constrained to $\beta_d = [3\pi/2, 2\pi)$, and the optimal direction of arrival solution is obtained as $\Phi = 270°$. The Euclidean features on the stationary object are shown as blue (●). (For interpretation of the references to color in this figure legend, the reader is referred to the web version of this article.)

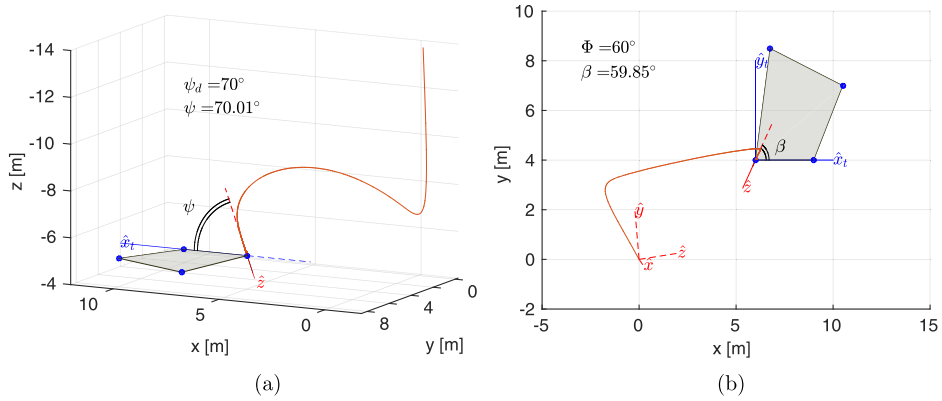

Fig. 10. Trajectory of the camera in the (a) 3D Euclidean space and (b) its projection on the *xy*-plane showing the achieved the angle of obliquity ψ and the direction of arrival β. The desired angle of obliquity is $\psi_d = 70°$, the desired direction of arrival β_d is singleton at $\beta_d = \pi/3$, and the direction of arrival solution is $\Phi = 60°$. The Euclidean features on the stationary object are shown as blue (●). (For interpretation of the references to color in this figure legend, the reader is referred to the web version of this article.)

of obliquity and from the desired direction of arrival, the following scenarios are considered. **Scenario 1.** While keeping the desired angle of obliquity at $\psi_d = 70°$, the direction of arrival is considered to be **(a)** unconstrained $\beta_d = [0, 2\pi)$; **(b)** constrained to a set of angles $\beta_d = [3\pi/2, 2\pi)$; and **(c)** singleton $\beta = \pi/3$. The results provide insights into the optimal direction of arrival solution and how it is enforced by the controller in Eqs. (26), (41), and (42). **Scenario 2.** The performance of the controller was verified when the angle of obliquity was varied from $\psi_d = 5°$ to $\psi_d = 85°$ in the increment of 10°, while maintaining $\beta_d = [0, 2\pi)$. **Scenario 3.** The singular case, when $\psi_d = \pi/2$, was considered to demonstrate the behavior of the system using the controller developed for the special case presented in Section 4.1.1.

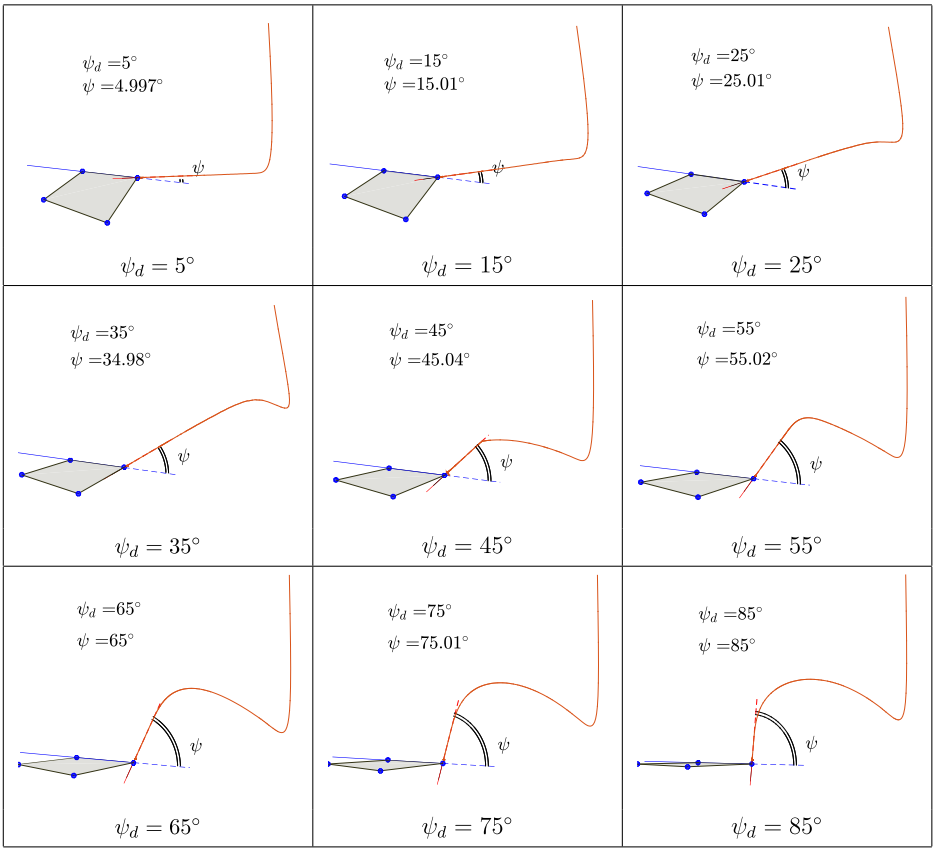

Fig. 11. Trajectories of the camera in the 3D Euclidean space showing the achieved angles of obliquity ψ for the desired angles of obliquity from $\psi_d = 5^\circ$ to $\psi_d = 85^\circ$, where the desired angle of arrival is unconstrained $\beta_d = [0, 2\pi)$. The Euclidean features on the stationary object are shown as blue (●). (For interpretation of the references to color in this figure legend, the reader is referred to the web version of this article.)

The objective of the translation controller in each of the above scenarios is to regulate the origin of the camera coordinate frame $\mathcal{F}$ to the Euclidean feature $\mathcal{O}_1$.

5.1. Preliminaries

Consider a local inertial frame $\mathcal{I}$. Then, the position $x_t^I \in \mathbb{R}^3$ and orientation $R_t^I \in \mathbb{R}^{3\times3}$ of the coordinate frame $\mathcal{F}_t$ attached to the stationary object with respect to $\mathcal{I}$ was considered to be

$$x_t^I = \begin{bmatrix} 6 & 4 & -5 \end{bmatrix}^T \text{ m}, \qquad R_t^I = \mathbf{I}_{3\times3} \tag{52}$$

where $\mathbf{I}_{3\times3}$ is an identity matrix. The position $x_*^I \in \mathbb{R}^3$ and orientation $R_*^I \in \mathbb{R}^{3\times3}$ of the auxiliary camera coordinate frame $\mathcal{F}^*$ (i.e., $\mathcal{F}|_{t=0}$) with respect to $\mathcal{I}$ was

$$x_*^I = \begin{bmatrix} 10 & 0 & -40 \end{bmatrix}^T \text{ m}, \tag{53}$$

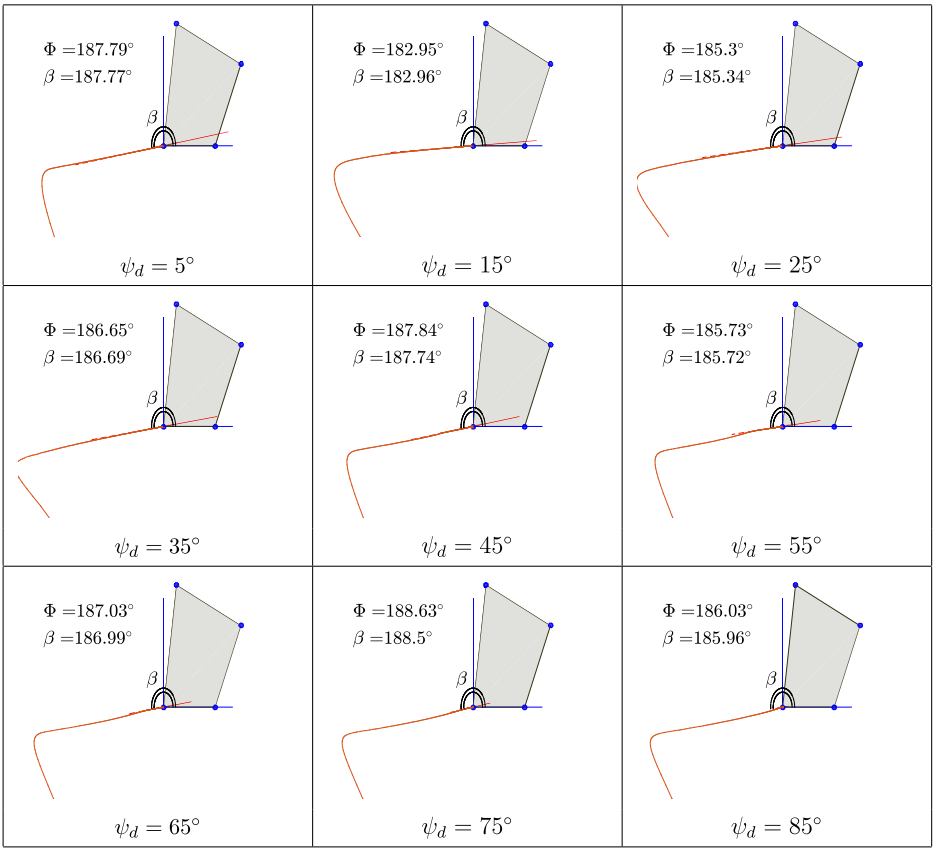

Fig. 12. Trajectories of the camera projected in the xy-plane showing the achieved direction of arrival β for the desired angles of obliquity from $\psi_d = 5^\circ$ to $\psi_d = 85^\circ$, where the desired angle of arrival is unconstrained $\beta_d = [0, 2\pi)$.

$$R_*^I = \begin{bmatrix} 0.2862 & -0.6718 & -0.6833 \\ 0.7106 & -0.3296 & 0.6217 \\ -0.6428 & -0.6634 & 0.3830 \end{bmatrix}. \tag{54}$$

The Euclidean features on the stationary object were considered to be in the xy-plane of $\mathcal{F}_t$. Without loss of generality, the feature $\mathcal{O}_1$ was considered to be at the origin of $\mathcal{F}_t$. The other features were at $\mathcal{O}_2 = [3, 0, 0]^T$, $\mathcal{O}_3 = [4.5, 3, 0]^T$, and $\mathcal{O}_4 = [0.75, 4.5, 0]^T$. The pixel coordinates of the features seen by the camera were assumed to be corrupted by white Gaussian noise of standard deviation 0.1pixel. The reference direction $\bar{\nu}$ in Definition 2 is considered to be the $+x$-axis of $\mathcal{I}$.

5.2. Results

The simulation results corresponding to the scenarios described previously are presented below. **Scenario 1(a).** $\psi_d = 70^\circ$, $\beta_d = [0, 2\pi)$. Fig. 6 shows the Euclidean trajectory of the camera along with plane π formed by four feature points on the stationary object. The 3D

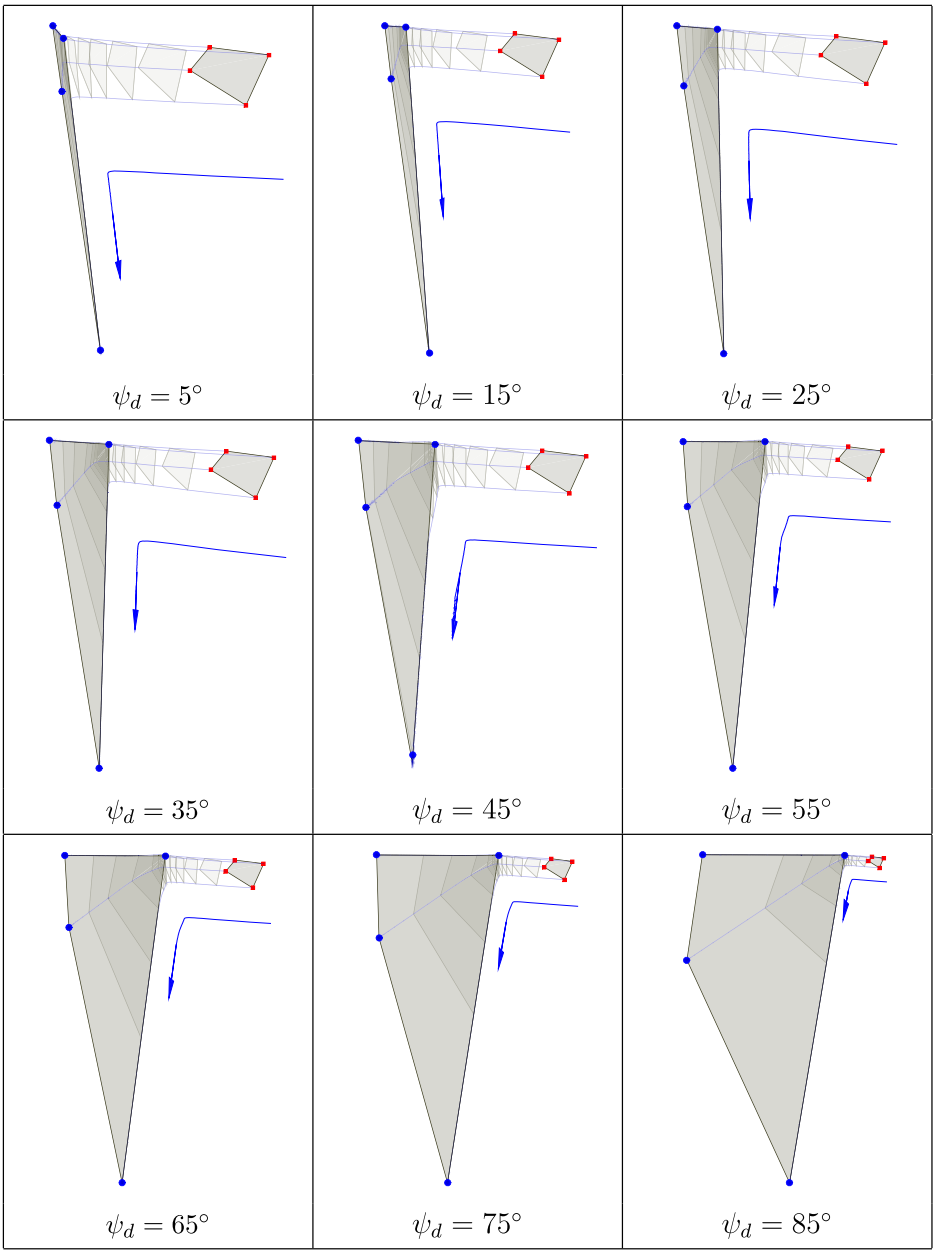

Fig. 13. Image-space trajectories of the feature points for the desired angles of obliquity from $\psi_d = 5^\circ$ to $\psi_d = 85^\circ$, where the desired angle of arrival is unconstrained $\beta_d = [0, 2\pi)$. The initial (at $t = t_0$) and the final (at $t = t_f$) positions of the features in the image are shown as red (■) and blue (●), respectively.(For interpretation of the references to color in this figure legend, the reader is referred to the web version of this article.)

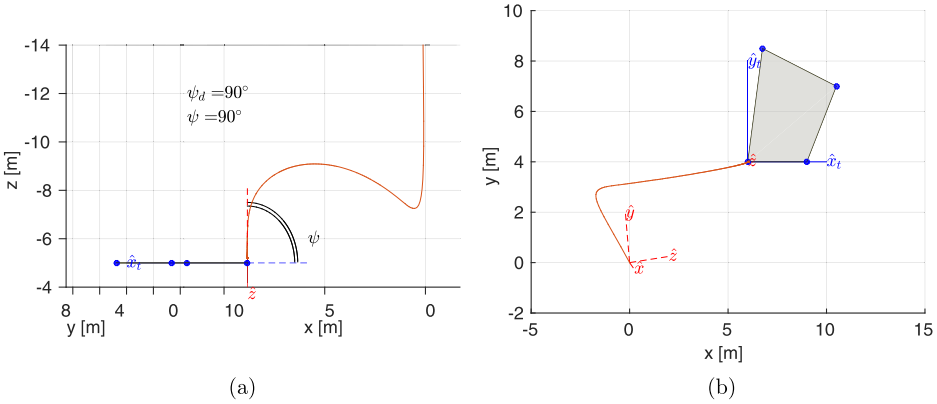

Fig. 14. Trajectory of the camera in the (a) 3D Euclidean space and (b) its projection on the xy-plane showing the achieved the angle of obliquity ψ. The desired angle of obliquity is $\psi_d = \pi/2$. The Euclidean features on the stationary object are shown as blue (●). (For interpretation of the references to color in this figure legend, the reader is referred to the web version of this article.)

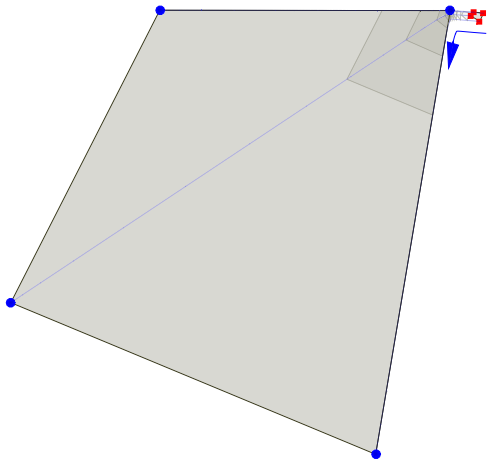

Fig. 15. Image-space trajectories of the feature points for the desired angles of obliquity $\psi_d = \pi/2$. The initial (at $t = t_0$) and the final (at $t = t_f$) positions of the features in the image are shown as red (■) and blue (●), respectively. (For interpretation of the references to color in this figure legend, the reader is referred to the web version of this article.)

Euclidean trajectory is shown in Fig. 6(a), while its projection on the xy-plane is shown in Fig. 6(b). Using the algorithm in Section 4, the optimal solution for the desired direction of arrival was obtained as $\Phi = 187°$. As shown in Fig. 6(a) and Fig. 6(b), the achieved angle of obliquity was $\psi(t_f) = 70.02°$ and direction of arrival was $\beta(t_f) = 187.04°$, where $t_f > 0$ denotes the final simulation time. The rotation and translation errors in Eqs. (23) and (36), respectively, are shown in Fig. 7, while the corresponding velocity control inputs are shown in Fig. 8. It can be seen from Figs. 7 and 8 that all control signals remain bounded at all times and reach zero in finite time.

Scenario 1(b). $\psi_d = 70°$, $\beta_d = [3\pi/2, 2\pi)$. Fig. 9 shows the Euclidean trajectory of the camera along with plane π formed by four feature points on the stationary object. The selected

β_d was such that $\beta \notin \beta_d$, therefore using Eqs. (17) and (18), the optimal solution was obtained to be $\Phi = 3\pi/2$. From Fig. 9(a) and 9(b), it can be observed that the achieved terminal angles were $\psi(t_f) = 70^\circ$ and $\beta(t_f) = 269.98^\circ$.

Scenario 1(c). $\psi_d = 70^\circ$, $\beta_d = \pi/3$. Fig. 10 shows the Euclidean trajectory of the camera along with plane π formed by four feature points on the stationary object. As discussed in the algorithm in Section 4, for singleton β_d, the optimal solution becomes $\Phi = \beta_d = \pi/3$. From Fig. 10(a) and 10(b), it can be observed that the achieved terminal angles were $\psi(t_f) = 70.01^\circ$ and $\beta(t_f) = 59.85^\circ$.

Hence, it follows that the optimal solution to the direction of arrival is obtained such that the optical axis coincides with the closest generatrix (permissible by β_d constraint) of the cone formed by the geometry of the terminal constraints. Subsequently, the rotation controller ensures that the orientation of the camera is regulated to satisfy the obtained optimal solution along with ψ_d.

Scenario 2. $\psi_d = 5^\circ$ to 85°, $\beta_d = [0, 2\pi)$. The desired angle of obliquity was varied from 5° to 85° in the increments of 10°, while maintaining the direction of arrival unconstrained. Fig. 11 shows the trajectory of the camera in the 3D Euclidean space, and also shows the achieved angle of obliquity $\psi(t_f)$ for each case. The optimal direction of arrival solutions, for the cases above, along with the achieved direction of arrival are shown in Fig. 12. Fig. 13 shows the image-space trajectory of the features $\mathcal{O}_1 \cdots \mathcal{O}_4$, where the initial (at $t = t_0$) and the final (at $t = t_f$) positions of the features in the image are shown as red '■' and blue '●', respectively. The figure also shows the plane π as viewed by the camera at various instances between t_0 and t_f.

Scenario 3. $\psi_d = \pi/2$. The objective is to orient the camera such that the optical axis is normal to the plane π. As discussed in Section 4.1.1, β_d cannot be defined for this singular case. The 3D trajectory of the camera in Fig. 14(a) demonstrates that the developed controller achieves $\psi(t_f) = \pi/2$. Fig. 15 shows the image-space trajectory of the features.

6. Conclusion

A new paradigm in visual servo control is presented, where a reference image may not available to determine the camera's relative pose and evaluate control signals. Motivated by practical applications, such as robotic fruit harvesting and manufacturing processes, a visual servo control problem is formulated by introducing the notions of angle of incidence and direction of arrival that lead to establishing terminal constraints on the pose of the camera. A constrained convex optimization problem is formulated and an efficient algorithm solution is provided to identify the orientation that minimizes the camera motion while satisfying terminal constraints. Further, continuous terminal sliding mode controllers are developed for the rotation and translation sub-systems, and Lyapunov-based stability analysis guarantees that the origin is a finite-time-stable equilibrium of the sub-systems. The applications that can benefit from the presented controller include: missile/smart-munition guidance, robotic fruit harvesting, manufacturing automation, and robotic hazardous material handling.

There are multiple avenues for future work. First, we will extend this work to obtain an optimal solution for the desired direction of arrival by reformulating the optimization problem to not only consider the current orientation of the camera but also take into account its desired position (specifically, the line-of-sight vector to the desired position). An optimal solution to such problem will reduce the overall camera motion. Second, the future work may consider an uncalibrated camera to provide image measurements to robustify against

modeling uncertainties and provide a camera-independent approach. Lastly, the field-of-view (FOV) constraints will be included in the optimization model to design a tracking problem that will ensure that the object does not leave the camera's FOV.

References

[1] P.I. Corke, Visual control of robot manipulators – a review, in: Visual Servoing, World Scientific, 1994, pp. 1–31.
[2] S. Hutchinson, G. Hager, P. Corke, A tutorial on visual servo control, Robotics and Automation, IEEE Transactions on 12 (5) (1996) 651–670.
[3] P. Corke, S. Hutchinson, A new partitioned approach to image-based visual servo control, Robotics and Automation, IEEE Transactions on 17 (4) (2001) 507–515.
[4] E. Malis, Survey of vision-based robot control, in: ENSIETA European Naval Ship Design Short Course, 2002.
[5] E. Malis, F. Chaumette, S. Bodel, 2 1/2 D visual servoing, Robotics and Automation, IEEE Transactions on 15 (2) (1999) 238–250.
[6] K. Deguchi, Optimal motion control for image-based visual servoing by decoupling translation and rotation, in: Proc. IEEE/RSJ Int. Conf. Intell. Robots Syst., 1998, pp. 705–711.
[7] G. Morel, T. Liebezeit, J. Szewczyk, S. Boudet, J. Pot, Explicit incorporation of 2d constraints in vision based control of robot manipulators, Experimental Robotics VI (2000) 99–108.
[8] E. Malis, F. Chaumette, 2 1/2 d visual servoing with respect to unknown objects through a new estimation scheme of camera displacement, International Journal of Computer Vision 37 (1) (2000) 79–97.
[9] E. Malis, F. Chaumette, Theoretical improvements in the stability analysis of a new class of model-free visual servoing methods, IEEE Transactions on robotics and automation 18 (2) (2002) 176–186.
[10] Y. Fang, A. Behal, W. Dixon, D. Dawson, Adaptive 2.5D visual servoing of kinematically redundant robot manipulators, in: Decision and Control, Proceedings of the 41st IEEE Conference on, 3, 2002, pp. 2860–2865.
[11] Y. Fang, D.M. Dawson, W.E. Dixon, M.S. de Queiroz, 2.5D visual servoing of wheeled mobile robots, in: Proc. IEEE Conf. Decision Control (CDC), 2002, pp. 2866–2871.
[12] Y. Fang, W.E. Dixon, D.M. Dawson, J. Chen, Robust 2.5D visual servoing for robot manipulators, in: Proc. of the American Control Conf. (ACC), 2003, pp. 3311–3316.
[13] Y. Fang, W.E. Dixon, D.M. Dawson, P. Chawda, Homography-based visual servoing of wheeled mobile robots, IEEE Trans. Syst., Man, Cybern. - Part B: Cybern. 35 (5) (2005) 1041–1050.
[14] Y. Fang, W. Dixon, D. Dawson, J. Chen, An exponential class of model-free visual servoing controllers in the presence of uncertain camera calibration, International Journal of Robotics and Automation 21 (4) (2006) 247–255.
[15] J. Chen, A. Behal, D. Dawson, Y. Fang, 2.5 d visual servoing with a fixed camera, in: American Control Conference, 2003. Proceedings of the 2003, 4, IEEE, 2003, pp. 3442–3447.
[16] J. Chen, W.E. Dixon, M. Dawson, M. McIntyre, Homography-based visual servo tracking control of a wheeled mobile robot, IEEE Transactions on Robotics 22 (2) (2006) 406–415.
[17] G. Hu, W. MacKunis, N. Gans, W.E. Dixon, J. Chen, A. Behal, D. Dawson, Homography-based visual servo control with imperfect camera calibration, Automatic Control, IEEE Transactions on 54 (6) (2009) 1318–1324.
[18] G. Hu, N. Gans, N. Fitz-Coy, W. Dixon, Adaptive homography-based visual servo tracking control via a quaternion formulation, IEEE Transactions on Control Systems Technology 18 (1) (2010) 128–135.
[19] S. Mehta, W.E. Dixon, D. MacArthur, C.D. Crane, Visual servo control of an unmanned ground vehicle via a moving airborne monocular camera, in: Proceedings of the American Control Conference (ACC), 2006, pp. 5276–5281.
[20] S. Mehta, G. Hu, N. Gans, W. Dixon, Adaptive vision-based collaborative tracking control of an ugv via a moving airborne camera: A daisy chaining approach, in: Decision and Control, Proceedings of the 45th IEEE Conference on, 2006, pp. 3867–3872.
[21] S. Mehta, V. Jayaraman, T. Burks, W. Dixon, Teach by zooming: A unified approach to visual servo control, Mechatronics 22 (4) (2012) 436–443.
[22] K. Hashimoto, A review on vision-based control of robot manipulators, Advanced Robotics 17 (10) (2003) 969–991.
[23] S.S. Mehta, J.W. Curtis, A geometric approach to visual servo control in the absence of reference image, in: Systems, Man, and Cybernetics, Proceedings of the IEEE Conference on, 2011, pp. 3113–3118.
[24] M. Held, R. Fischer, Penetration theory for inclined and moving shaped charges, Propellants, Explosives, Pyrotechnics 11 (4) (1986) 115–122.

[25] W.P. Walters, W. Flis, P. Chou, A survey of shaped-charge jet penetration models, International Journal of Impact Engineering 7 (3) (1988) 307–325.
[26] S.S. Mehta, T.F. Burks, Vision-based control of robotic manipulator for citrus harvesting, Computers and Electronics in Agriculture 102 (2014) 146–158.
[27] S.S. Mehta, W. MacKunis, T.F. Burks, Robust visual servo control in the presence of fruit motion for robotic citrus harvesting, Computers and Electronics in Agriculture 123 (2016) 362–375.
[28] C.W. Bac, T. Roorda, R. Reshef, S. Berman, J. Hemming, E.J. van Henten, Analysis of a motion planning problem for sweet-pepper harvesting in a dense obstacle environment, Biosystems Engineering 146 (2016) 85–97.
[29] B. Herisse, T. Hamel, R. Mahony, F.-X. Russotto, The landing problem of a vtol unmanned aerial vehicle on a moving platform using optical flow, in: Intelligent Robots and Systems (IROS), 2010 IEEE/RSJ International Conference on, IEEE, 2010, pp. 1600–1605.
[30] P. Serra, R. Cunha, T. Hamel, D. Cabecinhas, C. Silvestre, Landing on a moving target using image-based visual servo control, in: Decision and Control (CDC), 2014 IEEE 53rd Annual Conference on, IEEE, 2014, pp. 2179–2184.
[31] H. Nomura, T. Naito, Integrated visual servoing system to grasp industrial parts moving on conveyer by controlling 6DOF arm, in: Systems, Man, and Cybernetics, 2000 IEEE International Conference on, 3, IEEE, 2000, pp. 1768–1775.
[32] D. Kragić, A.T. Miller, P.K. Allen, Real-time tracking meets online grasp planning, in: Robotics and Automation, 2001. Proceedings 2001 ICRA. IEEE International Conference on, 3, IEEE, 2001, pp. 2460–2465.
[33] Y. Wang, G.-l. Zhang, H. Lang, B. Zuo, C.W. De Silva, A modified image-based visual servo controller with hybrid camera configuration for robust robotic grasping, Robotics and Autonomous Systems 62 (10) (2014) 1398–1407.
[34] O. Faugeras, F. Lustman, Motion and structure from motion in a piecewise planar environment, International Journal of Pattern Recognition and Artificial Intelligence 2 (3) (1988) 485–508.
[35] O. Faugeras, Three-Dimensional Computer Vision, The MIT Press, Cambridge Massachusetts, 2001.
[36] S. Yu, X. Yu, B. Shirinzadeh, Z. Man, Continuous finite-time control for robotic manipulators with terminal sliding mode, Automatica 41 (11) (2005) 1957–1964.
[37] S.P. Bhat, D.S. Bernstein, Lyapunov analysis of finite-time differential equations, in: American Control Conference, Proceedings of the 1995, 3, IEEE, 1995, pp. 1831–1832.
[38] P. Garnell, D.J. East, Guided Weapon Control Systems, Oxford: Pergamon Press, 1977.
[39] P. Zarchan, Tactical and strategic missile guidance. Progress in astronautics and aeronautics, 176, New York: AIAA, 1998.
[40] D. Karagiannis, A. Astolfi, A new solution to the problem of range identification in perspective vision systems, IEEE Transactions on Automatic Control 50 (12) (2005) 2074–2077.
[41] A. Dani, N. Fischer, Z. Kan, W.E. Dixon, Globally exponentially stable observer for vision-based range estimation, Mechatron. 22 (4) (2012) 381–389.
[42] A. Dani, N. Fisher, W.E. Dixon, Single camera structure and motion, IEEE Trans. Automat. Control 57 (1) (2012) 241–246.